Supporting Information

Interfacial Engineering of Cobalt Phosphide Heterostructures Confined in N, P-Doped Carbon for Efficient Bifunctional Electrocatalysis in Zn-Air Battery

Zongxu Li [a], Yonghang Zeng [a], Dongbin Xiong [a], Lina Zhou [a], Jianqing Zhou [a], Yahui Yang [d], Faqi Zhan [e], Kai Wang [b], Yue Du [a*], Yisi Liu [a, c*]

[a] College of Materials Science and Engineering & Hubei Key Laboratory of Photoelectronic Conversion Materials and Devices, Hubei Normal University, Huangshi, 435002, China

[b] Hubei Key Laboratory of Pollutant Analysis and Reuse Technology, College of Urban and Environmental Sciences, Hubei Normal University, Huangshi 435002, China

[c] Laboratory of Solid State Microstructures, Nanjing University, Nanjing 210093, China

[d] National & Local Joint Engineering Laboratory for New Petro-chemical Materials and Fine Utilization of Resources, College of Chemistry and Chemical Engineering, Hunan Normal University, Changsha, 410081, China

[e] State Key Laboratory of Advanced Processing and Recycling of Non-Ferrous Metals, Lanzhou University of Technology, Lanzhou 730050, China

*Corresponding author. Tel.: +86 18772289593

E-mail address: duyue_1991@126.com (Y. Du); yliu88@hbnu.edu.cn (Y. Liu)

Materials characterization

The X-ray diffraction (XRD) patterns were acquired at room temperature using an X-ray diffractometer (D/Max2500, Rigaku Corporation) with Cu Kα radiation (λ = 1.5406 Å). The morphology and structure of the samples were observed on field-emission scanning electron microscope (FESEM, GeminiSEM 300) and Transmission electron microscopy (TEM) measurements were proceeded on a FEI Tecnai F20 with an acceleration voltage of 120 kV. N_2 adsorption-desorption isotherms were measured using the Micromeritics ASAP 2460 analyzer. Raman spectrum was recorded on a HORIBA Evolution Raman Microscope spectrometer with the excitation wavelength of 532 nm. X-ray photoelectron spectrum (XPS) measurements was carried out on a Thermo Fisher Scientific 1063 X-ray photoelectron spectrometer with Al Kα radiation and the binding energies were calibrated based on the graphite C 1s peak (284.8 eV). The pyrolysis experiments were performed in a sensitive thermobalance (Perkin-Elmer, Pyris1 TGA) at a heating rate of 10 ℃/min up to a final temperature of 600 ℃ under the helium flow rate of 50 mL/min. A quadrupole mass spectrometer (Perkin-Elmer, Clarus 500 MS) coupled to the thermobalance was used for the evolved gas analysis. To avoid secondary reactions, a probe was placed very close to the sample pan of the thermobalance in the direction of the gas flow. The transfer lines between the TGA and MS were heated to 200 ℃ in order to avoid cold spots and thus prevent the condensation of the gaseous products. The evolving rates of the gaseous products were estimated from the measurements.

Electrochemical measurements

The electrochemical measurements were conducted on the Princeton electrochemical workstation and rotating disk electrode equipment (Pine Instruments Co. Ltd. USA) with a three-electrode system at room temperature. Graphite rod and Ag/AgCl (3 M KCl) were served as the counter and reference electrode, respectively. The electrolyte was 0.1 M KOH solution. The catalyst ink was prepared as our previous work [1]: 4 mg of catalyst was dispersed in 15 μL of 5 wt.% Nafion and 300 μL of isopropyl alcohol solution, then ultrasonicated for 1 h to obtain a well-dispersed catalytic ink. 10 μL of catalyst ink was dropped on the rotating disk glassy carbon electrode (5 mm in diameter, pine instrument) and dried by an infrared lamp. The catalyst loading was approximately 0.65 mg cm^{-2}.

The cyclic voltammograms (CVs) were recorded from −1.2 to 0.2 V (*vs.*Ag/AgCl) at a scan rate of 50 mV s^{-1} for ten cycles until the steady state cyclic voltammogram curves reached. The linear sweep voltammograms (LSVs) for ORR were recorded from 0.2 to −1.0 V (*vs.*Ag/AgCl) at a scan rate of 5 mV s^{-1} with various rotation rates from 400 to 1600 rpm. The LSVs for OER were recorded from 0.0 to 1.0 V (*vs.*Ag/AgCl) at a scan rate of 5 mV s^{-1} with the rotation rate of 1600 rpm. The electrolyte was aerated using high-purity O_2 for 0.5 h before each test and O_2 was maintained during the test. The potentials were converted to the reversible hydrogen electrode (RHE) by using the equation $E_{RHE} = E_{Ag/AgCl} + 0.197 + 0.0591pH$. The onset potential is defined as the potential when the ORR current density reaches 1% of the limiting diffusion current density.

Density functional theory (DFT) calculations

All the DFT calculations were conducted based on the Vienna Ab-inito Simulation Package (VASP) [2, 3]. The exchange-correlation effects were described by the Perdew-Burke-Ernzerhof (PBE) functional within the generalized gradient approximation (GGA) method [4, 5]. The core-valence interactions were accounted by the projected augmented wave (PAW) method [6]. The energy cutoff for plane wave expansions was set to 450 eV, and the 3×3×1 Monkhorst-Pack grid k-points were selected to sample the Brillouin zone integration. The vacuum space is adopted 15 Å above the surfaces to avoid periodic interactions. The structural optimization was completed for energy and force convergence set at 1.0×10^{-4} eV and 0.02 eV $Å^{-1}$, respectively.

The Gibbs free energy change (ΔG) of each step is calculated using the following formula:

$$\Delta G = \Delta E + \Delta ZPE - T\Delta S$$

where ΔE is the electronic energy difference directly obtained from DFT calculations, ΔZPE is the zero point energy difference, T is the room temperature (298.15 K) and ΔS is the entropy change. ZPE could be obtained after frequency calculation by [7]:

$$ZPE = \frac{1}{2}\sum hvi$$

And the TS values of adsorbed species are calculated according to the vibrational frequencies [8]:

$$TS = k_B T \left[\sum_k ln\left(\frac{1}{1 - e^{-hv/k_B T}}\right) + \sum_k \frac{hv}{k_B T} \frac{1}{\left(e^{hv/k_B T} - 1\right)} + 1 \right]$$

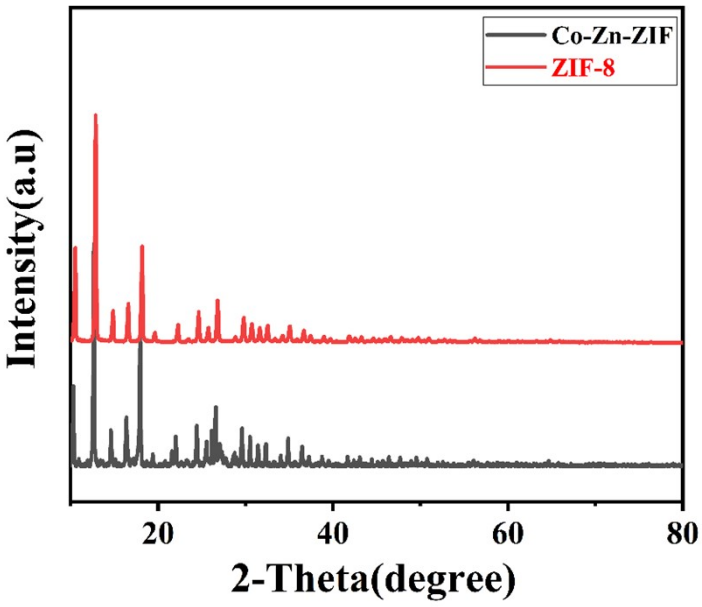

Fig.S1. The XRD pattern of ZIF-8 and Co/Zn-ZIF.

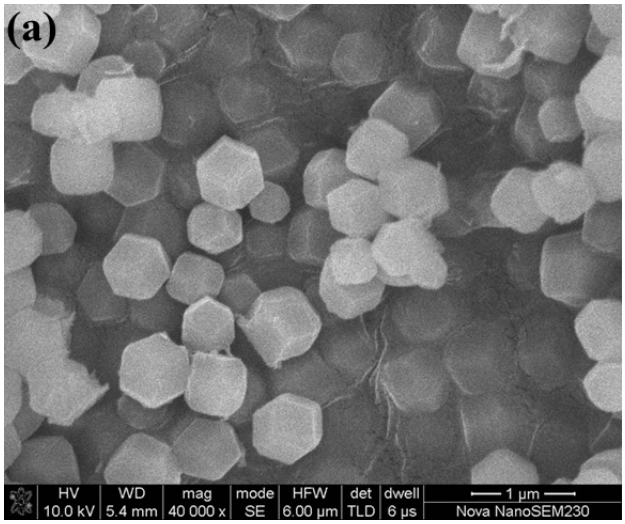

Fig. S2. The SEM image of ZIF-8.

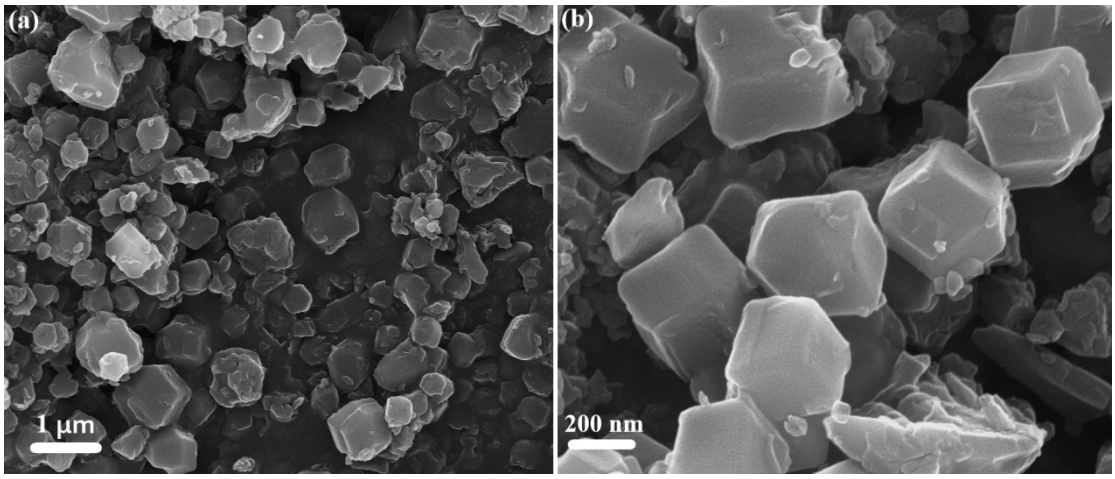

Fig. S3. The SEM images of Co/Zn-ZIFs at different magnifications.

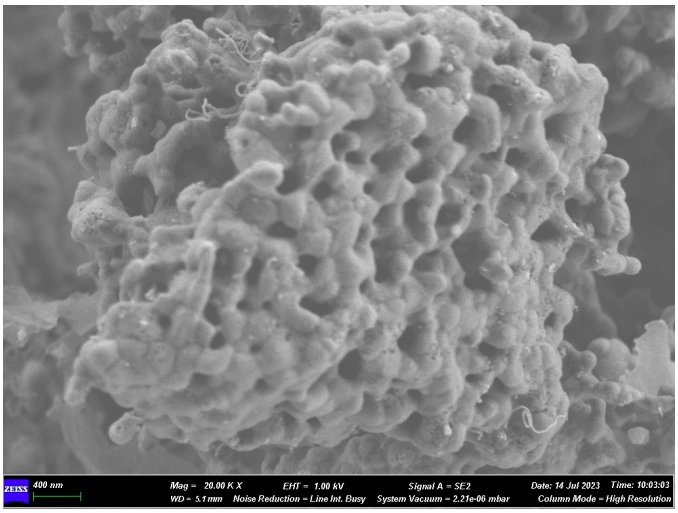

Fig. S4. The SEM image of Co_2P/NPC-0.1.

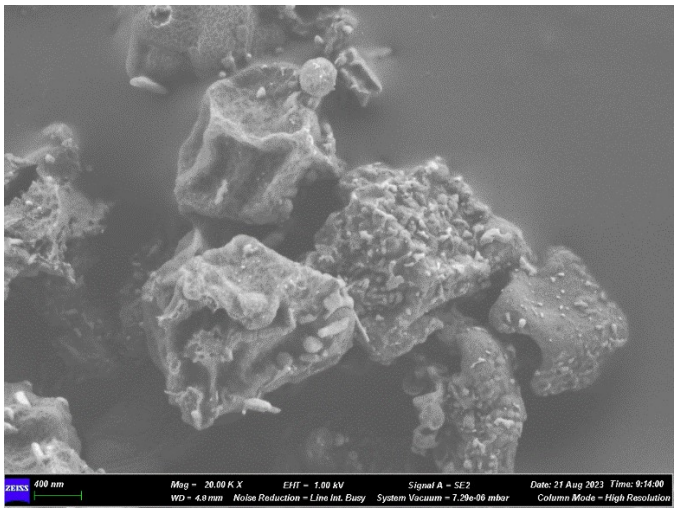

Fig. S5. The SEM image of Co_2P/NPC-0.3.

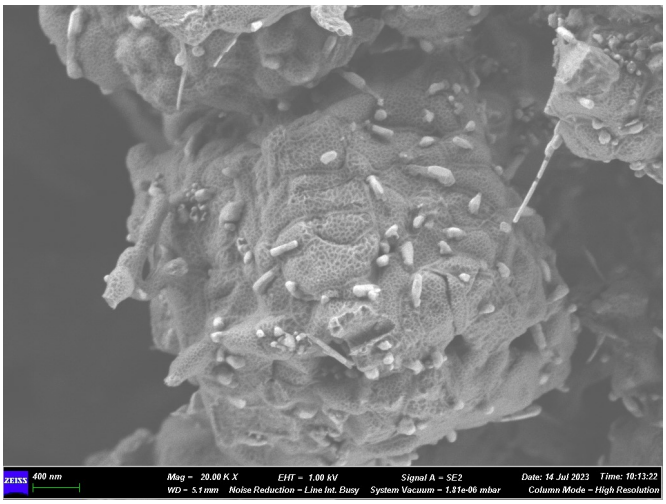

Fig. S6. The SEM image of CoP/NPC-2.

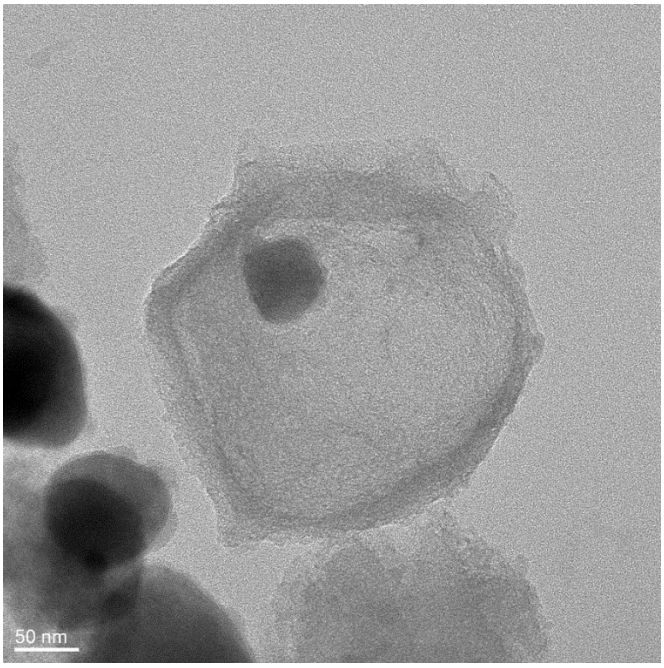

Fig. S7. The TEM image of CoP@Co_2P/NPC-0.5.

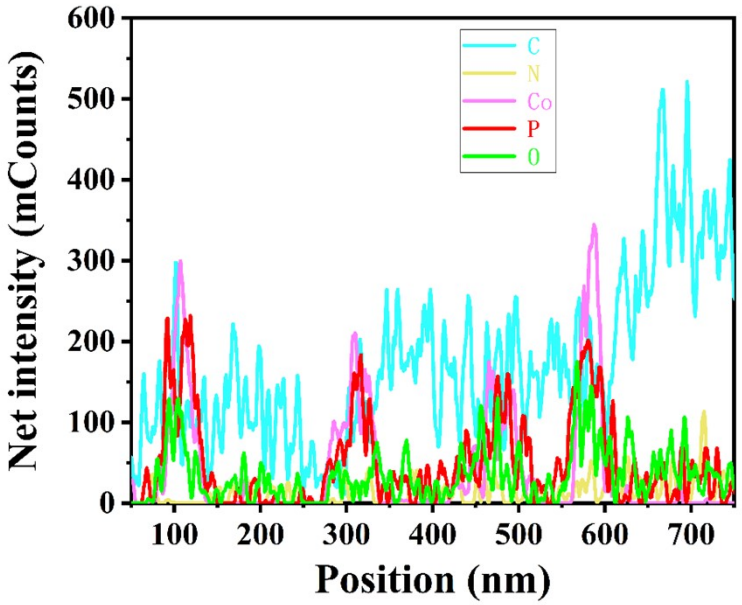

Fig. S8. The EDS linear scan profile of C, N, Co, O, and P.

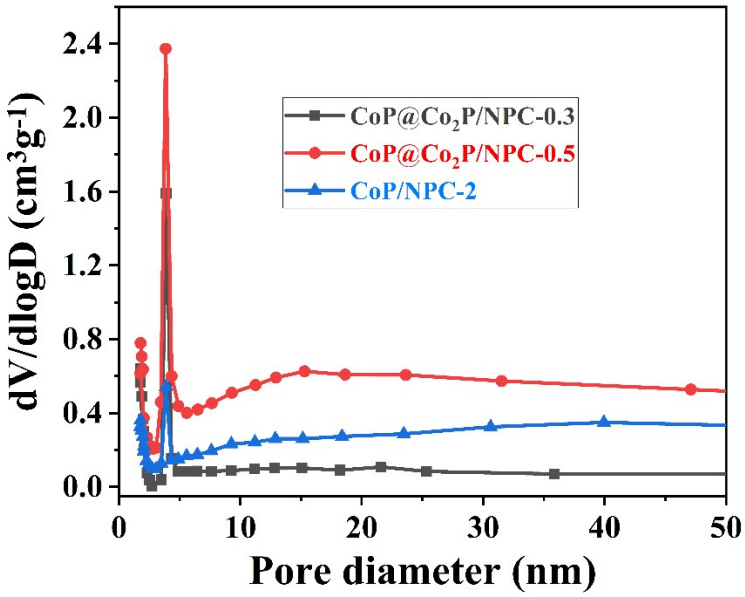

Fig. S9. The pore-size distributions of CoP@Co_2P/NPC-0.3, CoP@Co_2P/NPC-0.5, and CoP/NPC-2.

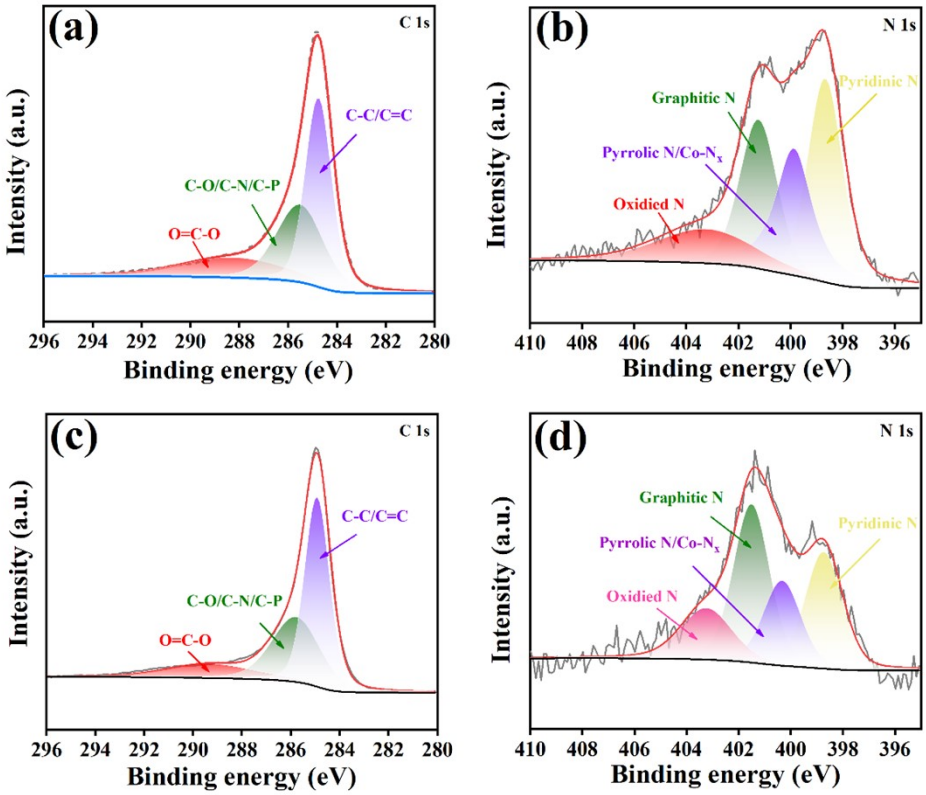

Fig. S10. The high-resolution XPS spectrums of (a, c) C 1s, (b, d) N 1s for CoP@Co_2P/NPC-0.3 and CoP/NPC-2.

Table S1. The peak area ratio of four nitrogen species in the N 1s high-resolution spectra for CoP@Co_2P/NPC-0.3, CoP@Co_2P/NPC-0.5 and CoP/NPC-2.

	CoP@Co_2P/NPC-0.3	**CoP@Co_2P/NPC-0.5**	**CoP /NPC-2**
	Peak area %	**Atomic %**	**Atomic %**
pyridinic N	32.61	31.48	27.09
pyrrolic N/Co-N_x	25.78	10.92	20.18
graphitic N	26.28	38.20	36.46
oxidized N	15.33	19.40	16.27

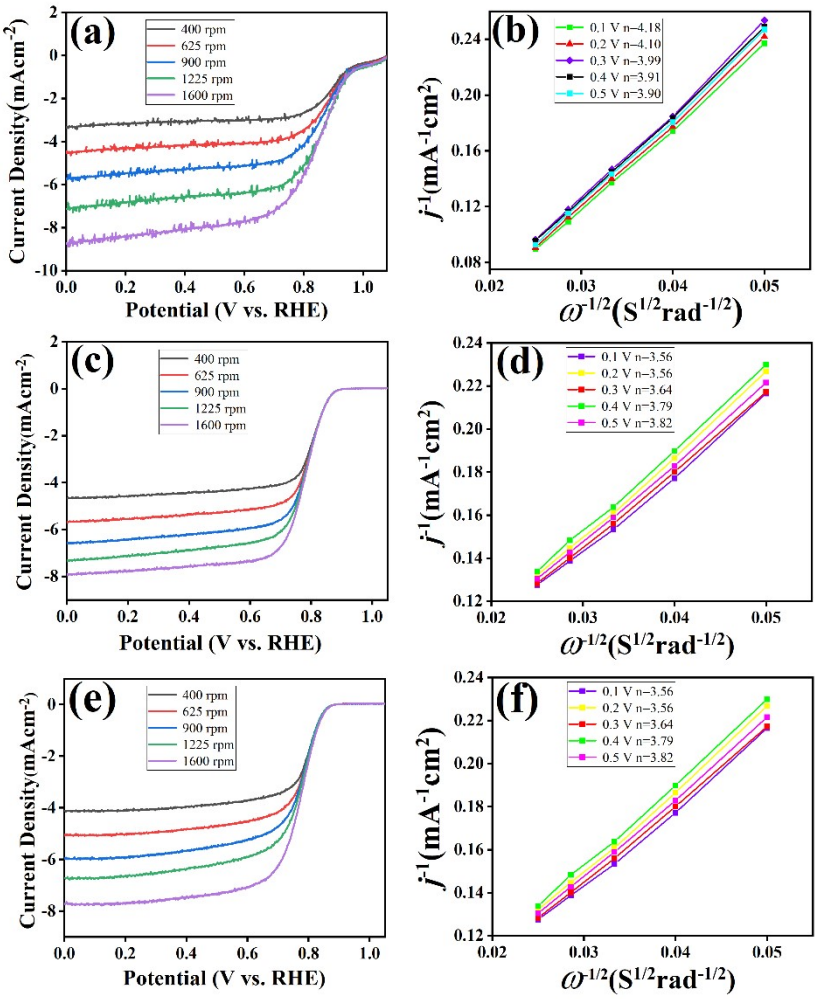

Fig. S11. The LSV curves in O_2-saturated 0.1 M KOH solution at various rotation rates and corresponding Koutecky-Levich plots at different potentials of (a, b) Co_2P/NPC-0.1, (c, d) CoP@Co_2P/NPC-0.3 and (e, f) CoP/NPC-2.

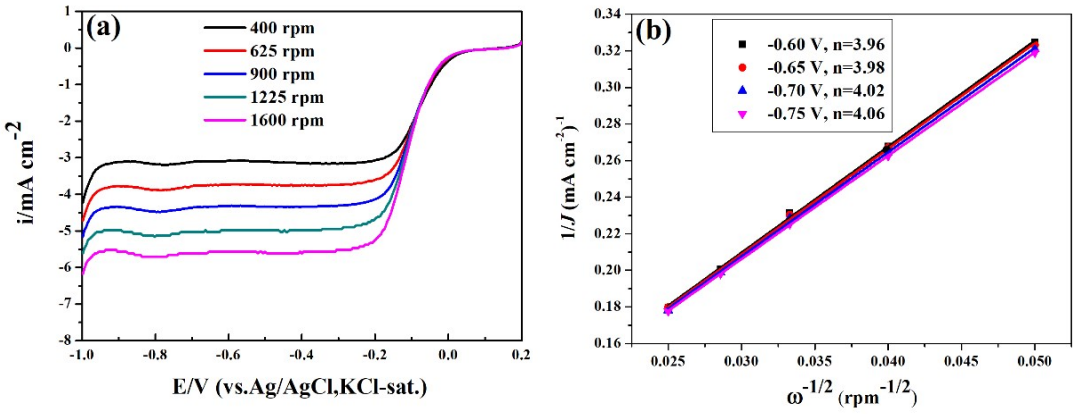

Fig. S12 (a) The LSV curves of Pt/C in O_2-saturated 0.1 M KOH solution at various rotation rates; (b) Corresponding Koutecky-Levich plots at different potentials.

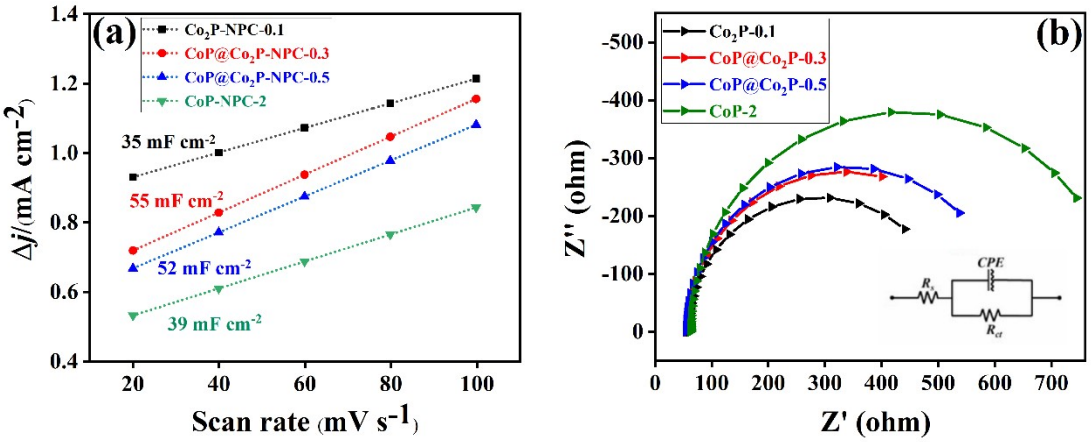

Fig. S13. (a) Plots showing the extraction of the C_{dl}; (b) Nyquist plots of Co_2P/NPC-0.1, CoP@Co_2P/NPC-0.3, CoP@Co_2P/NPC-0.5, and CoP/NPC-2.

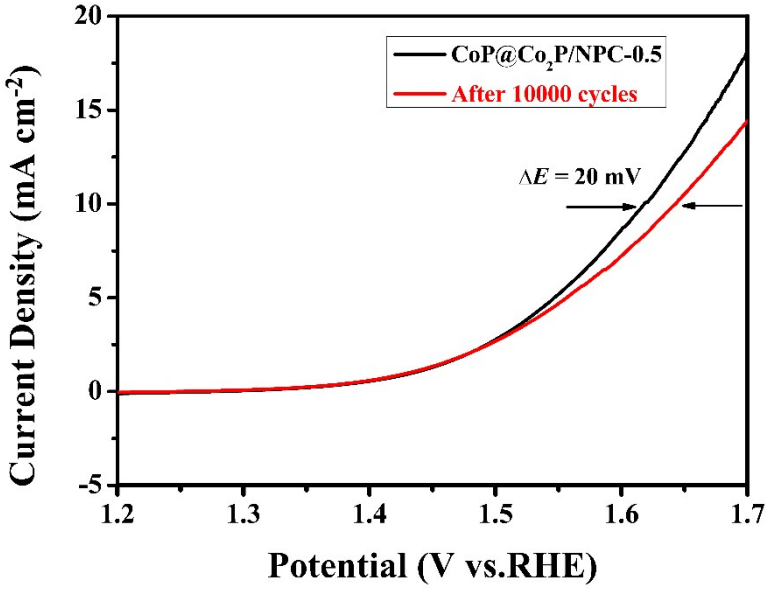

Fig. S13. The stability test for OER at 1600 rpm in O_2-saturated 0.1 M KOH solution after 10000 CV cycles.

Table S2 Comparison of bifunctional catalytic activity of the catalysts in this work with the recently reported noble-metal phosphide based catalysts in alkaline solution[a].

			E_{OER} at 10		ΔE (V)	
$E_{1/2}$ (*vs.* RHE)	E_{onset} (*vs.* RHE)	Tafel slope (mV dec^{-1})	mA cm^{-2} (*vs.* RHE)	Tafel slope (mV dec^{-1})		Ref

CoP@Co_2P/NPC-0.5	0.83	0.92	71.94	1.61	94.40	0.79	This work
Co_2P/Co-N-C	0.82	0.98	102	1.65	115	0.83	[9]
Cu-Co_2P/CNFs	0.778	undefined	95.2	1.60	87.3	undefined	[10]
Co_2P/doped-CNTs	0.843	0.91	55	1.573	96.1	0.814	[11]
Fe-Co_2P@NPDC	0.895	1.059	91	1.55	61	0.655	[12]
Co_2P/CoP@NPGC-1	0.93	0.986	69	1.57	116	0.64	[13]
Co/Co_2P@NPCNTs	0.88	1.00	55.4	1.54	71.5	0.66	[14]
Co_xP@NPC	0.83	undefined	undefined	1.55	87	0.75	[15]
Co_2P@NPCNTs-900	0.80	0.94	68.9	1.59	62.4	undefined	[16]
Co_2P@NCNTs-15	0.82	0.90	73	1.74	151	0.93	[17]
Co_2P/NPC	0.84	0.92	45.9	1.55	59.6	0.78	[18]

[a] All the potentials values above are converted to *vs*. RHE for comparison. In 0.1 M KOH electrolyte (pH=13), E(*vs*. RHE) = E(*vs*. Ag/AgCl) + 0.197 V + 0.0591pH.

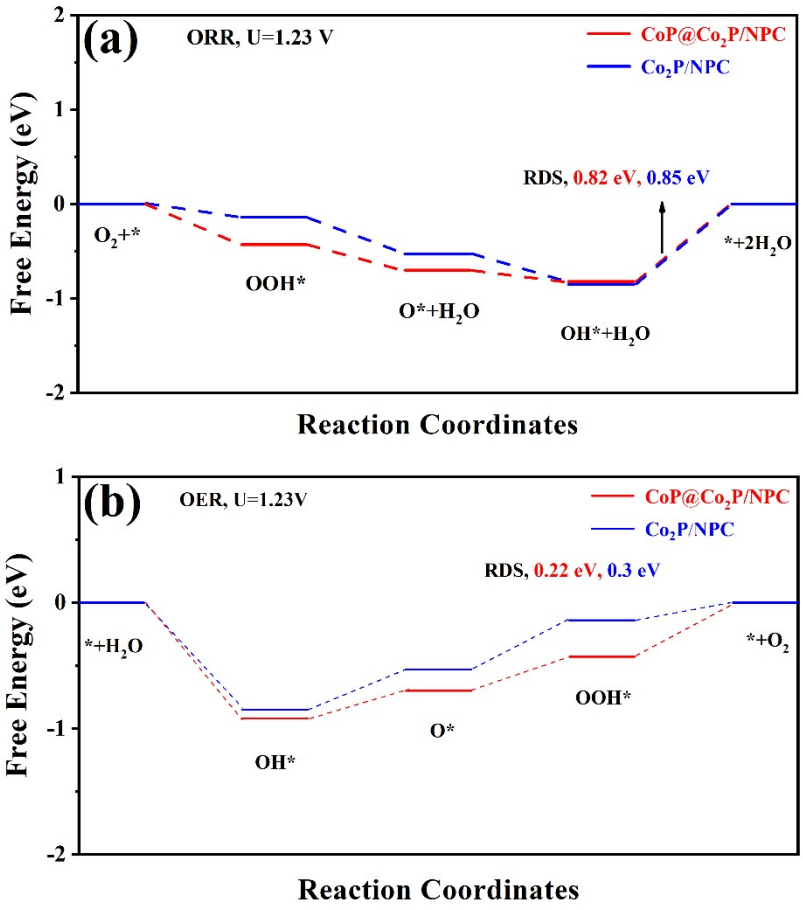

Fig. S15. Free energy diagrams for ORR and OER on CoP@Co_2P/NPC and CoP/NPC at electrode potential U=1.23 V.

Table S3. Performances of recently reported Zn-air batteries based on bi-functional catalysts.

	Open-circuit voltage (V)	**Peak power density (mW cm^{-2})**	**Durability**	**Ref (year)**
yolk-shell Co-N-C@GNP	1.60	236.2	Over 94 hours@ 5 mA/cm^2	This work
Pt/C+RuO_2	1.50	203.1	91 h@5 mA/cm^2	This work

Co-NCNT	1.42	44	30 hours@ 2 mA/cm^2	[19]
N-doped CNT arrays embedded with confined Co nanoparticles	1.40	44.8	2000 min@1 mA cm^{-2}	[20]
Activated carbon cloth	1.367	52.3	1000 min@1 mA cm^{-2}	[21]
MnO_x/carbon cloth	1.427	32	66 h@0.7 mA cm^{-2}	[22]
N doped graphene quantum dots engineered 3D $NiCo_2S_4$ nanoarray/ carbon cloth	1.4	26.2	500 h@25 mA cm^{-2}	[23]
CNT fibers	1.31	undefined	80 min@1 mA cm^{-2}	[24]
Fe-Co_4N@N-C	1.34	72	45 cycles@4 mA cm^{-2}	[25]

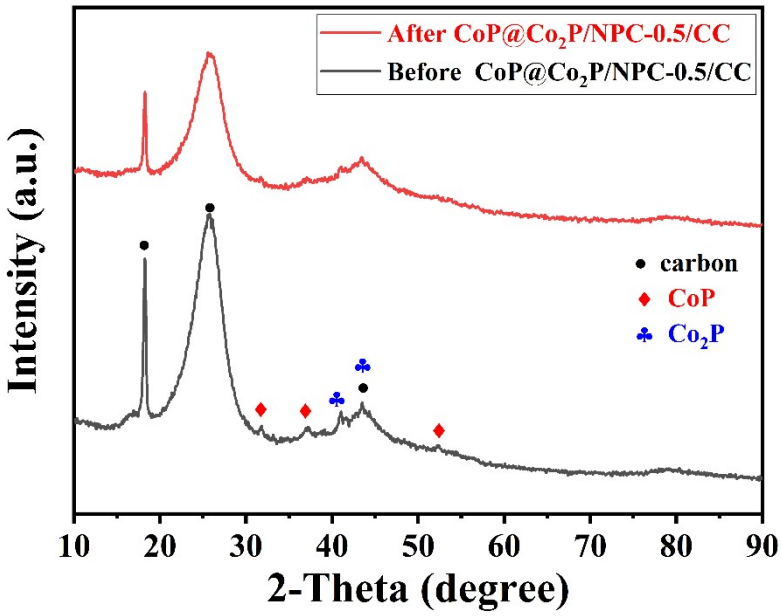

Fig. S16. The XRD spectra of CoP@Co_2P/NPC-0.5 before and after 30 recharging cycles in Zn-air battery.

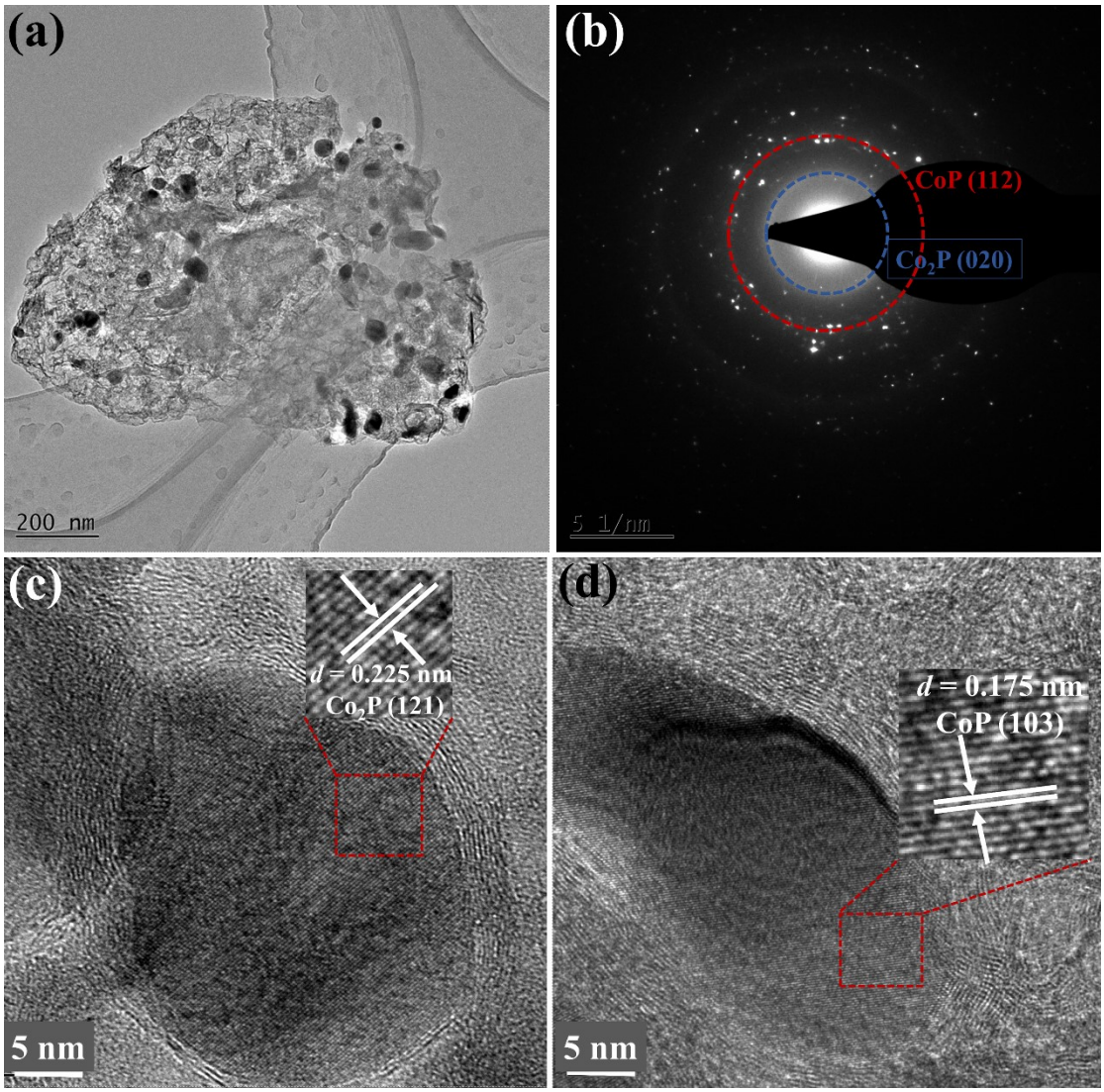

Fig. S17. (a) The TEM image; (b) X-ray diffraction pattern (SAED); (c, d) The HRTEM images of CoP@Co_2P/NPC-0.5 after 30 recharging cycles in Zn-air battery.

References

[1] Y. Liu, Z. Chen, Z. Li, N. Zhao, Y. Xie, Y. Du, J. Xuan, D. Xiong, J. Zhou, L. Cai, Y. Yang, CoNi nanoalloy-Co-N4 composite active sites embedded in hierarchical porous carbon as bi-functional catalysts for flexible Zn-air battery, Nano Energy, 99 (2022) 134469.

[2] G. Kresse, J. Hafner, Ab Initiomolecular Dynamics for Liquid Metals, *Phys. Rev. B* 47 (1993) 558-561.

[3] G. Kresse, J. Hafner, Ab Initiomolecular-Dynamics Simulation of the Liquid-Metal-Amorphous-Semiconductor Transition in Germanium, *Phys. Rev. B* 49 (1994) 14251-14269.

[4] J. P. Perdew, K. Burke, M. Ernzerhof, Generalized Gradient Approximation Made Simple. *Phys. Rev. Lett.* 77 (1996) 3865-3868.

[5] G. Kresse, D. Joubert, From Ultrasoft Pseudopotentials to the Projector Augmented-Wave

Method. *Phys. Rev. B* 59 (1999) 1758-1775.
[6] P. E. Blöchl, Projector Augmented-Wave Method, *Phys. Rev. B* 50 (1994) 17953-17979.
[7] Nørskov JK, Rossmeisl J, Logadottir A, Lindqvist L, Kitchin JR, Bligaard T, Jonsson H. Origin of the overpotential for oxygen reduction at a fuel-cell cathode. J. Phys. Chem. B 108, 46 (2004) 17886–17892.
[8] Bendavid LI, Carter EA. CO_2 Adsorption on Cu_2O(111): A DFT+U and DFT-D Study, J. Phys. Chem. C 117, 49 (2013) 26048–26059.
[9] Q. Xu, X. Peng, Z. Zhu, K. Luo, Y. Liu, D. Yuan, Co2P nanoparticles supported on cobalt-embedded N-doped carbon materials as a bifunctional electrocatalyst for rechargeable Zn-air batteries, International Journal of Hydrogen Energy, 47 (2022) 16518-16527.
[10] X. Sun, H. Liang, H. Yu, J. Bai, C. Li, Embedding Co_2P nanoparticles in Cu doping carbon fibers for Zn–air batteries and supercapacitors, Nanotechnology, 33 (2022) 135202.
[11] L. Song, H. Fan, X. Fan, H. Gong, T. Wang, J. He, A simultaneous phosphorization and carbonization strategy to synthesize a defective Co_2P/doped-CNTs composite for bifunctional oxygen electrocatalysis, Chemical Engineering Journal, 435 (2022) 134612.
[12] L. Li, L. Zhang, Z. Nie, W. Ma, N. Li, T. Wågberg, G. Hu, Tailoring charge reconfiguration in dodecahedral Co_2P@carbon nanohybrids by triple-doping engineering for promoted reversible oxygen catalysis, Journal of Materials Chemistry A, 10 (2022) 21659-21671.
[13] W. Gong, H. Zhang, L. Yang, Y. Yang, J. Wang, H. Liang, Core@shell MOFs derived Co2P/CoP@NPGC as a highly-active bifunctional electrocatalyst for ORR/OER, Journal of Industrial and Engineering Chemistry, 106 (2022) 492-502.
[14] H. Yang, B. Wang, S. Kou, G. Lu, Z. Liu, Mott-Schottky heterojunction of Co/Co_2P with built-in electric fields for bifunctional oxygen electrocatalysis and zinc-air battery, Chemical Engineering Journal, 425 (2021) 131589.
[15] Q. Shi, Q. Liu, Y. Zheng, Y. Dong, L. Wang, H. Liu, W. Yang, Controllable Construction of Bifunctional Co_xP@N,P-Doped Carbon Electrocatalysts for Rechargeable Zinc–Air Batteries, Energy & Environmental Materials, 5 (2021) 515-523.
[16] Q. Shao, T. Li, H.-g. Wang, Y. Li, Z. Si, Q. Duan, A facile one-pot synthesis of Co_2P nanoparticle-encapsulated doped carbon nanotubes as bifunctional electrocatalysts for high-performance rechargeable Zn–air batteries, CrystEngComm, 23 (2021) 1013-1018.
[17] X. Peng, Y. Liu, S. Hu, P. Zheng, Y. Fu, P. Dong, J. Xiao, L. Han, Y. Zhang, Synthesis of a highly efficient bifunctional Co_2P@N-doped carbon nanotubes electrocatalyst by GO-Induced assembly strategy for rechargeable Zn-air batteries, Journal of Alloys and Compounds, 889 (2021) 161628.
[18] D. Zhang, P. Sun, Z. Zuo, T. Gong, N. Huang, X. Lv, Y. Sun, X. Sun, N, P-co doped carbon nanotubes coupled with Co2P nanoparticles as bifunctional oxygen electrocatalyst, Journal of Electroanalytical Chemistry, 871 (2020) 114327.
[19] Q. Lu, X. Zou, K. Liao, R. Ran, W. Zhou, M. Ni, Z. Shao, Direct growth of ordered N-doped carbon nanotube arrays on carbon fiber cloth as a free-standing and binder-free air electrode for

flexible quasi-solid-state rechargeable Zn-Air batteries, Carbon Energy, 2 (2020) 461-471.
[20] C. Zhu, Y. Ma, W. Zang, C. Guan, X. Liu, S.J. Pennycook, J. Wang, W. Huang, Conformal dispersed cobalt nanoparticles in hollow carbon nanotube arrays for flexible Zn-air and Al-air batteries, Chemical Engineering Journal, 369 (2019) 988-995.
[21] K. Kordek, L. Jiang, K. Fan, Z. Zhu, L. Xu, M. Al-Mamun, Y. Dou, S. Chen, P. Liu, H. Yin, P. Rutkowski, H. Zhao, Two-Step Activated Carbon Cloth with Oxygen-Rich Functional Groups as a High-Performance Additive-Free Air Electrode for Flexible Zinc–Air Batteries, Advanced Energy Materials, 9 (2018) 1802936.
[22] A. Sumboja, M. Lübke, Y. Wang, T. An, Y. Zong, Z. Liu, All-Solid-State, Foldable, and Rechargeable Zn-Air Batteries Based on Manganese Oxide Grown on Graphene-Coated Carbon Cloth Air Cathode, Advanced Energy Materials, 7 (2017).
[23] W. Liu, B. Ren, W. Zhang, M. Zhang, G. Li, M. Xiao, J. Zhu, A. Yu, L. Ricardez-Sandoval, Z. Chen, Defect-Enriched Nitrogen Doped-Graphene Quantum Dots Engineered NiCo2 S4 Nanoarray as High-Efficiency Bifunctional Catalyst for Flexible Zn-Air Battery, Small, 15 (2019) e1903610.
[24] A. Pendashteh, J. Palma, M. Anderson, J.J. Vilatela, R. Marcilla, Doping of Self-Standing CNT Fibers: Promising Flexible Air-Cathodes for High-Energy-Density Structural Zn–Air Batteries, ACS Applied Energy Materials, 1 (2018) 2434-2439.
[25] Q. Xu, H. Jiang, Y. Li, D. Liang, Y. Hu, C. Li, In-situ enriching active sites on co-doped Fe-Co4N@N-C nanosheet array as air cathode for flexible rechargeable Zn-air batteries, Applied Catalysis B: Environmental, 256 (2019) 117893.